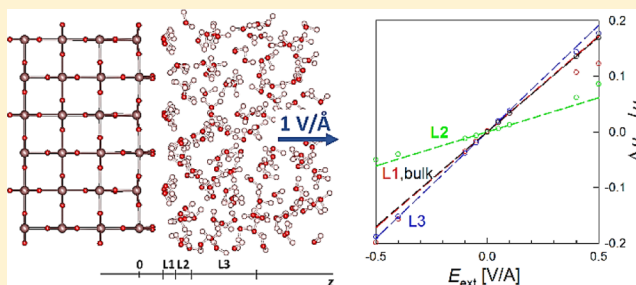


Dielectric Properties of Water at Rutile and Graphite Surfaces: Effect of Molecular Structure

Stanislav Parez,^{*,†} Milan Předota,^{†,‡} and Michael Machesky[§][†]Institute of Chemical Process Fundamentals, Academy of Sciences of the Czech Republic, Prague, 165 02, Czech Republic[‡]Faculty of Science, University of South Bohemia, Branisovska 1760, Ceske Budejovice, 370 05, Czech Republic[§]University of Illinois, State Water Survey, 2204 Griffith Drive, Champaign, Illinois 61820, United States

ABSTRACT: The dielectric properties of interfacial water adjacent to the surfaces of hydrophobic graphite and the 110 surface of hydrophilic rutile (α -TiO₂) are investigated by means of nonequilibrium molecular dynamics simulations. The dielectric behavior of water is found to arise from its local density and molecular polarizability in response to an external field, and can be rationalized in terms of the number and strength of water–surface and water–water H-bonds. The interplay of local density and polarizability leads to a particularly strong dielectric response, exceeding the external field, of the water layer directly contacting the surfaces, while the second layer exhibits a reduced response. Consequently, dielectric profiles near surfaces cannot be correctly described by implicit solvent models valid for bulk water. The overscreening response of the contact water layer has been observed in previous simulation studies and implies the local permittivity (dielectric constant) of that layer is negative. However, the negative permittivity of the contact water layer is counterbalanced by the positive permittivities of the surface depletion layer and the second water layer such that the calculated Stern layer capacitance is positive and compatible with experimental data. Moreover, the electrostatic potential profile matches well the profile calculated for an aqueous salt solution at the charged rutile (110) surface, thus supporting the “water centric” view of aqueous electrical double layers.



1. INTRODUCTION

Molecular dynamics (MD) simulations can provide valuable information about the structure and dynamics of water, ions, and molecules at the solid–liquid interface. Mineral surfaces contacting pure water only have been the subject of most previous MD simulations and include titanium dioxide,^{1,2} clay,³ carbonate,⁴ and sulfide⁵ minerals. Simulations in which mineral surfaces are in contact with both water and ions are rarer but include clay minerals,^{6,7} cassiterite (SnO₂),⁸ and gibbsite.⁹

The (110) rutile (α -TiO₂) surface in contact with aqueous solutions has been studied by MD simulation in our previous papers. The interfacial structure of water and ions from those simulations agrees very well with experimental data obtained by X-ray standing wave and X-ray reflectivity (e.g., crystal truncation rod) analysis of surface structures at ambient conditions,^{10–14} which can be treated as validation of our simulations and enables us to extend the range of investigated properties. In the ongoing research, we have studied diffusivity,¹⁵ shear viscosity,¹⁶ and hydrogen-bonding structure^{17,16} of the rutile–water interfacial region. The results demonstrate that interfacial properties can differ significantly from bulk behavior, which in turn questions continuum theories in which bulk values or bulk dependences are used in place of local counterparts.

This Article continues our investigation of rutile–aqueous solution interfacial phenomena by addressing dielectric proper-

ties. Our goal is to characterize the relative permittivity (dielectric constant) profile in the inhomogeneous region formed at the solid–liquid interface, as it changes from bulk values far from the surface to the vicinity of the surface. Moreover, our aim was not to calculate the “dielectric function” with a submolecular resolution, as in recent simulation studies,¹⁸ but to determine the permittivity of individual molecular layers of water at the surface. The reasons are 2-fold. First, permittivity is a quantity established in continuum theories of dielectrics to approximate electrostatic properties of a macroscopic volume in a polarizable solvent. We consider this concept reasonable on the scale exceeding or at least equal to a molecular length. Second, local permittivity can be analyzed in terms of other structural properties of the molecular layers. To that end, we will provide a molecular level explanation for the permittivity profile of water at the (strongly hydrophilic) rutile (110) surface, as well as the hydrophobic graphite surface for comparative purposes.

Direct measurements of interfacial permittivity are difficult due to the small thickness of the region over which permittivity varies. Dielectric spectroscopy provides dielectric relaxation spectra over a range of frequencies. Despite the signal

Received: December 31, 2013

Revised: February 11, 2014

Published: February 12, 2014

originating both from interfacial and from bulk environments, spectra can be decomposed into components corresponding to processes with different relaxation times, and the contribution of interfacial water can be assigned.^{19,20} However, the inferred value of interfacial permittivity depends on the proper interpretation of experimental spectra. Recently, terahertz spectroscopy has been introduced as a tool for directly probing interfacial water dynamics, and experiments on carbohydrates²¹ and lipid membranes²² have shown that the dielectric response of water is modified within a few solvation layers. Atomic force microscopy for water at mica surfaces was applied by Teschke et al.,²³ and their results showed a slow decrease in permittivity extending over ~ 25 nm as the surface was approached. In contrast, spectroscopic measurements (e.g., ref 21) and molecular simulations (e.g., ref 18) show permittivity varies only over a distance of a few molecular lengths. Bernik and Negri^{24,25} studied the local polarity of phospholipid vesicles by analyzing the Stokes shift of fluorescent probes. They observed anomalous values of permittivity, such as negative or extremely large values around 100, at the phospholipid–water interface. However, the anomalous values were interpreted as a spurious result due to uncertainties in estimating the local refractive index.

Obstacles to the detailed measurement of interfacial permittivity have resulted in the development of theoretical approaches and molecular simulations. Dielectric properties are frequently discussed in the framework of the electrical double layer (EDL) and its various constructs.^{26–29} A widely used construct is the Stern (or Gouy–Chapman–Stern) model,^{30,31} which partitions an interface into two layers: (i) the Stern layer (or Helmholtz layer), referring to the compact layer of immobile ions adsorbed at the surface, and (ii) the diffuse layer where the ions are mobile and their concentration profile obeys the Poisson–Boltzmann equation.^{32,33} The role of water is that of a continuum with relative permittivity $\epsilon_{r,i}$ filling the layer i . The model is parametrized with a Stern layer capacitance value, which is commonly fit to experimental surface titration data.^{27,29,34} For metal oxide surfaces in contact with 1:1 electrolyte solutions, Stern layer capacitance values can also be predicted with the empirical relationships developed by Sverjensky,^{35,36} which are strictly valid for the triple layer (two Stern layers and a diffuse layer) surface complexation model. Capacitance values were predicted to vary with both electrolyte type and oxide surface considered, with capacitance values for the innermost Stern layer ranging from about 0.5 to 1.6 F/m².

Values of permittivity do not follow directly from modeled capacitances, but can be linked to information on the positions of the Stern layers from X-ray reflectivity and other techniques according to the equation $C_i = \epsilon_r \epsilon_0 / d_i$, where C_i and d_i are the capacitance and thickness of layer i , respectively. Stern layer permittivity values derived from EDL models vary between ~ 6 for metal electrodes to 20–60 for metal oxides.^{29,35} However, because permittivity values are sensitive to the particular model applied,^{27,29,34} knowledge of interfacial permittivity via other methods would enable the assessment of various EDL models.

Classical EDL models are examples of “implicit solvent models”, which describe electrostatic profiles of water on a basis of mean field approximations (while the electrostatic potential arising from ions is often accounted for explicitly). Specifically, in the Poisson–Boltzmann equation used for the calculation of the total electrostatic profile, electrostatic potential is related to an explicit ionic charge distribution (assuming pointwise or finite size ions), whereas the electrostatic potential generated by

water is accounted for by a prescribed permittivity profile. Several formulas for calculating permittivity profiles of water can be found in the literature, from a simple constant bulk value to distance- or field-dependent permittivity.^{31,37–39} However, these formulas, for example, permittivity variance with electric field, were derived for homogeneous bulk systems, and these implicit solvent models completely ignore the effect of interfacial interactions on dielectric properties. The main goal of this Article is to show that the interfacial solvent and bond network structure indeed affect electrostatics, and to compare the effect to the behavior in homogeneous solution.

Simulation studies of interfacial dielectric properties have primarily addressed pure water at neutral surfaces, and differ in the simplicity of the molecular models used. For the simplest case of a smooth dielectric wall, dielectric profiles can be calculated semianalytically.⁴⁰ More complex surface models involve silica^{41,42} or membrane bilayers.^{43–45} A system similar to the present one, the quartz–water interface, was examined under different hydration levels by Wander and Clark.⁴⁶ They found permittivity to monotonously decrease toward the surface in agreement with the EDL picture, for example, ref 36. However, they calculated permittivity using the Kirkwood fluctuation formula,^{47,48} where correlations between individual water dipoles at zero external field appear. The plausibility of using this approach for interfaces is questionable at best. First, this approach is strictly applicable to homogeneous isotropic bulk fluids assuming the studied system is symmetrically surrounded by a dielectric medium.⁴⁷ Second, when applied to a water layer within the interfacial region, correlations with dipoles outside the layer are neglected, although their contribution might be substantial if water is strongly ordered. Third, contributions from dipole moment fluctuations due to molecules entering/leaving a particular layer are not properly addressed. These drawbacks were addressed by Ballenegger and Hansen,⁴⁹ who derived a correct fluctuation formula applicable to planar interfaces and calculated the permittivity (tensor) for a simple model of a dipolar liquid at a homogeneous dielectric wall. Bonthuis et al.^{18,50} generalized the fluctuation formula for the case of fluid molecules containing higher multipole moments and applied the formula to more realistic SPC/E water adjacent to planar, atomistically modeled, hydrophilic and hydrophobic diamond surfaces. Application of the correct fluctuation formula revealed a novel feature in the electrostatic profile: the local electric field in the contact water layer had a sign opposite to that of the external field.^{49,50} This “overscreening” of the external field by the dielectric response ultimately results in a negative value of permittivity (applied to the transverse component, i.e., perpendicular to the interface). Bonthuis et al. employed the permittivity profile in the Poisson–Boltzmann equation and succeeded in roughly matching experimental double layer capacitances as a function of electrolyte concentration.^{18,50} However, the comparison was done against experimental capacitance data from various carbon-based surfaces (including diamond) that were highly variable with respect to electrolyte concentration. In addition, calculated capacitance values and their concentration dependence were highly dependent on the definition of the surface charge position.⁵⁰ Still, calculated capacitances were similar for hydroxylated (hydrophilic) and nonhydroxylated (hydrophobic) diamond surfaces, and it was concluded that the corresponding electrostatic profiles were dominated by water rather than ionic contributions. We will confirm the latter conclusion based on explicit calculations of electrostatic profiles

from simulations of aqueous salt solutions at charged rutile surfaces.

Previous simulation studies on interfacial permittivity profiles have utilized pure solvent simulations, thereby neglecting the effect of ions on permittivity. We will examine simulations of a charged rutile surface in contact with NaCl electrolyte to determine whether the electrostatic profile reflects primarily ionic or intrinsic water properties by calculating the ionic and water contributions to the electrostatic profile explicitly from the simulation. However, determination of permittivity explicitly from such simulations is beyond the scope of this Article. For pure solvent systems (without free charges), the constitutive relation defining permittivity between displacement \mathbf{D} and electric \mathbf{E} fields is local:⁵¹ $\mathbf{D}(\mathbf{r}) = \epsilon_0 \epsilon_r(\mathbf{r}) \mathbf{E}(\mathbf{r})$, while if ions are included permittivity might show a nonlocal dependence.^{18,52} Generally, local permittivity is a good approximation when the displacement field varies slowly as compared to the electric field, that is, at low salt concentration. A simulation study of a realistic silica surface⁴² revealed nonlocal behavior of the dielectric function over the Stern layer, while the typical local permittivity description was adequate in the diffuse layer.

In this Article, we investigate the effect of water structure and local bonding on interfacial permittivity for two surfaces with a vastly different influence on the adjacent water: the strongly hydrophilic rutile (110) surface and a hydrophobic graphite surface. We first review the expressions used for calculating permittivity and use those expressions to determine permittivity in the molecular layers of interfacial water. Second, we give a molecular level explanation for the observed permittivity values. Local permittivity is related to density of a water layer and an orientational response of its molecules to the external field with the orientational response rationalized in terms of the local H-bonding structure. Third, values for the rutile surface are used to calculate the Stern layer capacitance and are compared to results from surface complexation modeling. In addition, the electrostatic profile from the simulation of a charged rutile surface is analyzed to determine the separate contributions of ions and water. Finally, we discuss the role of interfacial molecular structure for dielectric properties and the corresponding validity of implicit solvent models where structure is neglected.

2. METHODOLOGY

When a sample of a polar fluid is exposed to an external field \mathbf{E}_{ext} , it becomes polarized and produces a polarization field \mathbf{E}_p , which acts typically opposite to the external field. Let us consider a fluid confined in a slab under an external homogeneous electric field acting in the direction normal to the surfaces. The planar symmetry (neglecting effects due to roughness of the surfaces) ensures that the polarization field is nonzero only in its z -component, which is normal to the surface, $E_p \equiv E_p^z$. Its value can be derived from charge distribution or from multipole expansion. The charge distribution approach requires knowledge of the microscopic charge distribution ρ_q , such as the locations and magnitudes of partial charges that appear in Gauss's law:⁵¹

$$E_p(z) = \frac{1}{\epsilon_0} \int_{-\infty}^z \rho_q(z') dz' \quad (1)$$

where ϵ_0 is the permittivity of a vacuum and the coordinate z measures distance from a surface. In the multipole expansion

approach, the polarization field is generated by the polarization density vector \mathbf{P} :^{18,51}

$$\mathbf{E}_p(z) = -\frac{\mathbf{P}(z)}{\epsilon_0} \quad (2)$$

which comprises individual multipole density \mathbf{P}_i contributions:¹⁸

$$\mathbf{P}(z) = \mathbf{P}_1(z) - \nabla \cdot \mathbf{P}_2(z) + \nabla \nabla : \mathbf{P}_3(z) - \dots \quad (3)$$

The leading term of the expansion is the dipole moment density \mathbf{P}_1 . The equivalency of the charge density approach, eq 1, and the multipole expansion approach, eq 2, is ensured by the following relation:

$$P(z) = -\int_{-\infty}^z \rho_q(z') dz' \quad (4)$$

where $P \equiv P^z$.

The dielectric response of the sample (we will use the term "dielectric response" or "response" for the change in the polarization field ΔE_p on applying the external field; in a broader context, "response" can also refer to changes in microscopic structure of the sample driving the change in the polarization field) is often expressed via the relative permittivity ϵ_r . Assuming the local relation between polarization density and electric field, permittivity is defined through the linear constitutive relation:

$$\epsilon_r \epsilon_0 \mathbf{E} = \epsilon_0 \mathbf{E} + \mathbf{P} \quad (5)$$

where \mathbf{E} is the total electric field, that is, the sum of the external field and the polarization field:

$$\mathbf{E} = \mathbf{E}_{\text{ext}} + \mathbf{E}_p \quad (6)$$

According to eqs 2 and 5, polarization density is a linear function of the external electric field. This applies for small fields unless the polarization becomes saturated, whereby nearly all molecules are already aligned with the field and cannot react further by changing their orientation. For higher fields causing a nonlinear response, permittivity is allowed to be a function of the field to preserve the linear constitutive relation eq 5.

The definition of permittivity is more subtle when a system with an interface is considered, because a wall-induced polarization might exist even at a vanishing external field. As a result, polarization is no longer proportional to the external field. To describe the response of the fluid to the changes induced by the external field, the values of the polarization density and electric field in eq 5 are replaced by their changes $\Delta \mathbf{P}$ and $\Delta \mathbf{E}$ with respect to the reference values at zero external field:

$$\epsilon_r \epsilon_0 \Delta \mathbf{E} = \epsilon_0 \Delta \mathbf{E} + \Delta \mathbf{P} \quad (7)$$

By construction, $\Delta \mathbf{P}$ as well as $\Delta \mathbf{E} = \mathbf{E}_{\text{ext}} + \Delta \mathbf{E}_p$ vanish for a vanishing external field. The modified constitutive relation eq 7 thus enables comparison of permittivity in the bulk and at an interface for the same \mathbf{E}_{ext} . Note that outside the interfacial region the wall-induced polarization is zero as the bulk structure is recovered, and eq 7 reduces to the standard expression eq 5.

Considering the relation eq 2 between polarization and electric field, eq 7 leads to the following expression for permittivity:

$$\epsilon_r(z) = \frac{E_{\text{ext}}}{\Delta E(z)} = \frac{E_{\text{ext}}}{E_{\text{ext}} + \Delta E_p(z)} = \frac{1}{1 - SF(z)} \quad (8)$$

where we have introduced the screening factor $SF \equiv -\Delta E_p/E_{\text{ext}}$, which is a dimensionless factor describing that portion of the external field that is screened by the polarization field. In particular, $SF = 0$ if $\Delta E = E_{\text{ext}}$ (no screening of the external field, $\epsilon_r = 1$), while $SF = 1$ if $\Delta E = 0$ (complete screening of the external field, $\epsilon_r = \infty$).

Note that eq 8 is valid for the external electric field acting perpendicularly to the walls. Unlike in the bulk where longitudinal permittivity $\epsilon_r^{\parallel} = 1 + P^*/\epsilon_0 E_{\text{ext}}$ derived for the electric field that acts parallel to surfaces yields the same value (ref 53 for water), permittivity in the interfacial region is anisotropic^{18,49} due to fluid–surface interaction.

Permittivity can also be calculated on the basis of linear response theory⁴⁷ from molecular fluctuations of the system without the applied external field. This approach leads for homogeneous isotropic fluids to the well-known Kirkwood fluctuation formula:^{47–49}

$$\frac{(\epsilon_r - 1)(2\epsilon_r + 1)}{\epsilon_r} = \frac{1}{\epsilon_0 V k_B T} (\langle \mathbf{M}^2 \rangle_0 - \langle \mathbf{M} \rangle_0^2) \quad (9)$$

where k_B denotes the Boltzmann constant, T is the absolute temperature, \mathbf{M} is the total dipole moment of molecules in the volume V , and $\langle \dots \rangle_0$ denotes the ensemble average for zero external field. For slab geometry, the correct fluctuation formula is^{18,49}

$$\epsilon_r^{-1}(z) = 1 - \frac{1}{\epsilon_0 k_B T} (\langle P(z)M \rangle_0 - \langle P(z) \rangle_0 \langle M \rangle_0) \quad (10)$$

where $M \equiv \mathbf{M}^z = \int P(z) dV$.

3. SIMULATIONS

MD simulations of water slabs for a range of external homogeneous electric fields in the z direction were performed using our own parallel simulation code.

The TIP4P/2005 molecular model of water by Abascal and Vega⁵⁴ was employed. It consists of one Lennard-Jones (LJ) site and three point charges. This model is one of the most successful among the rigid nonpolarizable water models with respect to various structural and transport properties.⁵⁵ Using the molecular model, charge density and the dipole moment density vector were calculated bin-wise as

$$\rho_q(z) = \frac{1}{V_b} \sum_{\{i,\alpha\} \in V_b} q_{i,\alpha} \quad \mathbf{P}_1(z) = \frac{1}{V_b} \sum_{i \in V_b} \sum_{\alpha} q_{i,\alpha} \mathbf{r}_{i,\alpha} \quad (11)$$

where V_b is the volume of the parallel bin out to distance z from the surface, and $q_{i,\alpha}$ and $\mathbf{r}_{i,\alpha}$ are the charge, and position vector of site α at water molecule i , respectively. In the first equation, the summation runs over all sites within V_b , while in the latter equation, only water molecules with their center of mass (COM) inside V_b contribute.

To see the effect of different water–wall interactions, two different types of walls were considered, a graphite wall and a rutile (110) wall. The interaction between water and the graphite wall was described by the LJ 9-3 potential:

$$U(z_{\text{COM}}) = 4\pi\epsilon_0\sigma^3 \left[\frac{(\sigma/z_{\text{COM}})^9}{45} - \frac{(\sigma/z_{\text{COM}})^3}{6} \right] \quad (12)$$

where z_{COM} is the distance of the water molecule center of mass from the wall. The values of interaction parameters $\sigma = 3.28$ Å and $\epsilon/k_B = 51.08$ K and the number density of carbon atoms $\rho_w = 112.9125$ nm^{−3} were taken from ref 56. The rutile (110) wall, detailed in our previous works,^{10,57} represents a more realistic surface. This all-atom model reflects the structure of neutral nonhydroxylated rutile (110) surface.¹⁰ Wall atom positions were held rigid because no significant effects of surface flexibility were expected. The rutile wall consisted of four TiO layers, where the two deepest maintained the strictly periodic bulk crystal structure, while the other two were ab initio relaxed.⁵⁷ The surface is terminated by rows of bridging oxygens that protrude out from the 110 surface plane. The interaction parameters between the rutile wall and water are based on the ab initio-derived potentials.^{10,57} These potentials describe Ti–O(water) interactions in terms of Buckingham potentials, while the O(wall)–O(water) interaction is given by the LJ potential.

The applied external electric field E_{ext} values were ± 0.05 , ± 0.1 , ± 0.4 , ± 0.5 , ± 0.9 , ± 1 , ± 1.4 , and ± 1.5 V/Å. The weakest field applied was ± 0.1 V/Å for the graphite wall and ± 0.05 V/Å for the rutile wall. Weaker applied fields resulted in polarization changes from zero-external-field values comparable to statistical uncertainty, and hence of poor accuracy. The results for $\pm E_{\text{ext}}$ were obtained from a single simulation, because in each case the external field was oriented parallel to the surface normal of one surface, but antiparallel to the surface normal of the opposite surface. A positive field is taken to point toward the fluid phase (see Figure 1).

Simulations were carried out for 3000 water molecules. The unit simulation cell was a rectangular prism with a base parallel to the surface of area 35.5×39.0 Å². These dimensions were chosen to match 12×6 replicas of the rutile (110) unit cell. The separation of the two opposing walls in the z direction was adjusted so that the density of water in the bulk region was 1.0 g/cm³. The number of water molecules, density, and unit cell dimensions resulted in a slab thickness L of almost 70 Å. Because the inhomogeneous interfacial region extends typically to about 15 Å from the surface, the bulk phase length was nearly 40 Å.

Periodic boundary conditions were applied on the unit simulation cell in all three directions, and the three-dimensional Ewald summation technique with the dipole correction term (EW3DC) by Yeh and Berkowitz⁵⁸ was employed to treat long-range Coulombic interactions. This method yields an excellent agreement with the results from the rigorous two-dimensional Ewald summation technique^{47,58} while reducing computing time significantly. For optimal performance, a vacuum space of thickness 50–70 Å separated the nearest images in the z direction. The cutoff radius was set to 13 Å for both the LJ interaction and the real space Ewald summation.

Simulations were equilibrated over 10^6 time steps, followed by $\sim 6 \times 10^6$ time steps for production runs. The fifth-order Gear predictor-corrector integrator⁴⁷ was used to propagate the trajectories with a 0.9 fs time step. The temperature was controlled with the Nosé–Hoover thermostat.^{47,59,60} Predicted value statistical uncertainties were estimated with the block averaging method.⁶¹

4. RESULTS

4.1. Dielectric Properties of Molecular Layers. MD simulations of water confined between parallel rutile (110) and graphite walls were conducted at 298 K and 1 g/cm³ density. A

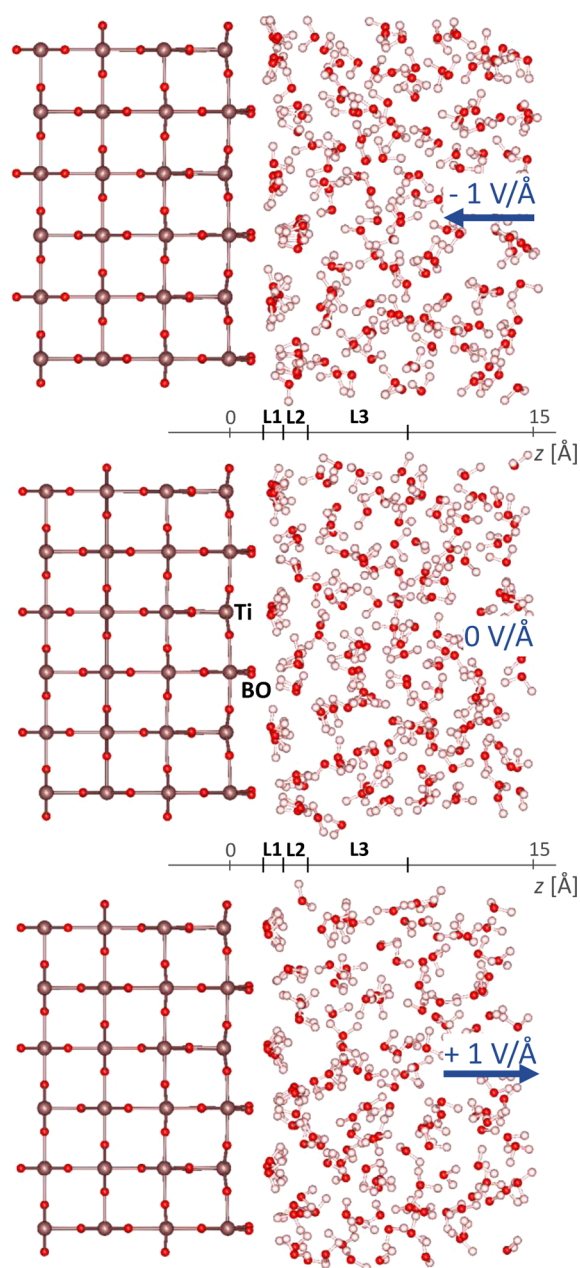


Figure 1. Snapshots from simulations of water at rutile wall for the external electric fields -1 , 0 , and 1 V/Å. A lateral look at a block of water molecules above 6×3 replicas of the rutile (110) unit cell is shown. Titanium atoms are gray, while oxygen atoms are red. In the middle panel, surface titanium (Ti) and bridging oxygen (BO) are denoted. Positions of water layers L1–L3 are also indicated.

strong external electric field was applied in the direction normal to the surfaces, and the response of the system was monitored. Particular attention was paid to the polarization changes of interfacial water layers to estimate their relative permittivities.

Interfacial polarization has its origin in a strong layering and preferential orientation of water in the vicinity of a surface, as shown in Figure 1. In Figure 2, the interfacial COM density (which is almost indistinguishable from the oxygen density) and hydrogen density profiles are plotted for the same external electric fields as in Figure 1 for the graphite and rutile surfaces. The position of the plane $z = 0$ corresponds to the position of Ti atoms in the interfacial Ti–O layer. Upon switching on a

strong external electric field, water molecules undergo substantial structural changes. While the effect of a homogeneous external field in the bulk phase is only alignment of molecular dipoles along the field (with no change in density), the interfacial structure also exhibits changes in local density, as a result of the inhomogeneous total electric field. Throughout the range of external fields applied, the changes in COM density profiles were mostly limited to narrowing and enhancing the density peaks. Thus, we can define a water layer as water molecules located between adjacent minima in COM density, the positions of which are independent of the applied external field. The reason for the latter requirement is that we will subtract polarization in a layer at zero external field from that at a finite field, and therefore it is more consistent to obtain both values from the same volume. The three studied layers, referred to as L1, L2, and L3, are indicated in Figure 2. The layers are of molecular width except for L3 at the rutile wall. For the strongest field strengths 1.4 and 1.5 V/Å, structural changes in some layers were too dramatic leading to deviations in the position and thickness of the layer with respect to the zero-field configuration. The results for these fields are not analyzed below.

For further determination of dielectric properties, it is essential to calculate polarization fields in the water layers defined above. In Figure 3, we compare polarization fields calculated by the charge density approach, equivalent to full multipole expansion, according to eq 1, and polarization fields generated by dipole moments only using eq 2 where the expansion of the polarization density vector 3 is restricted only to the dipole moment density \mathbf{P}_1 (calculated according to eq 11). The two profiles differ at the interface, particularly in the first two water layers. While the electric field is clearly not accurately described by the point dipoles approximation on a submolecular scale, we will compare the outcome of the electrostatic and dielectric approaches on a scale equal to or exceeding molecular dimensions, for which the point dipole approximation might become reasonable.

The mean polarization field E_{pi} in layer L_i , $i = 1, 2, 3$, or bulk water was calculated as the average value over the interval between layer boundaries, $E_{pi} = \langle E_p(z) \rangle_{L_i}$, where the polarization field profile $E_p(z)$ was taken as generated either by the dipole moment or by all multipole moments. Finally, to assess dielectric properties, the screening factor $SF \equiv -\Delta E_{pi}/E_{ext}$ cf., eq 8, based on the mean polarization fields within each layer, was calculated and is plotted in Figure 4 for the range of external fields. A surprising result is that some of the screening factor values are higher than 1. We will refer to this phenomenon as overscreening as it occurs when the magnitude of the polarization field response exceeds the magnitude of the external field. An ultimate consequence is a negative value of permittivity as defined by eq 8. The same phenomenon was found previously for a dipolar liquid at a dielectric wall⁴⁹ and for SPC/E water at a diamond surface.¹⁸

The differences between the dipole and full-multipole approaches, manifested by the difference between the respective profiles in Figure 3, are largely alleviated by the averaging procedure and subtraction of zero field values. Consequently, SF values are qualitatively similar for both approaches over the physically interesting range of small external fields. Nevertheless, for quantitative purposes, the full polarization field arising from all multipole contributions should be used.¹⁸ On the other hand, although the (atomistic) full-multipole approach gives a priori accurate profiles of the

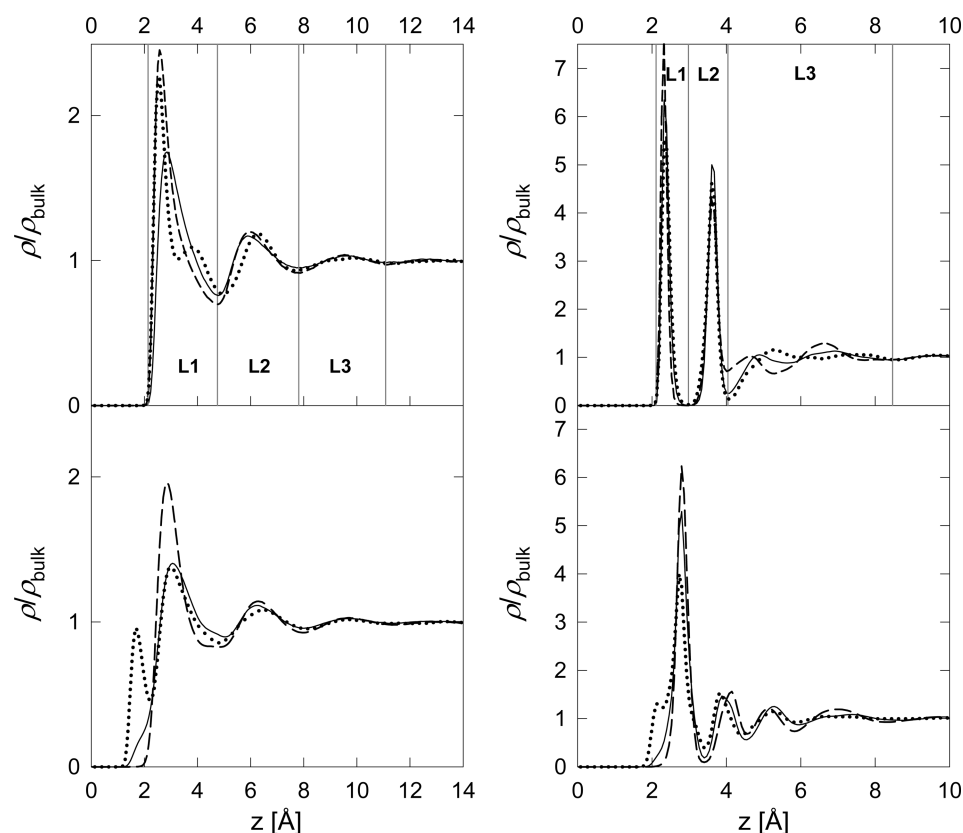


Figure 2. Center of mass (top) and hydrogen (bottom) density of interfacial water at graphite (left) and rutile (right) surfaces for the external electric fields -1 V/Å ($\bullet\bullet\bullet$), 0 V/Å ($-$), and 1 V/Å ($--$). The vertical lines in the top figures indicate boundaries of the L1, L2, and L3 water layers.

polarization field for a given model system, the resulting dielectric response is not unambiguously decomposed into distinct structural layer contributions (L1–L3) because the values of the electric field in a given layer, as calculated from the charge density, can include contributions from atoms of water molecules belonging to different layers. This effect is not present in the dipole moment approach where a contribution of a water molecule belongs entirely to the layer where the molecule COM is located.

The dielectric response is nonlinear over the entire range of applied fields for L1 and L2. Nevertheless, the smooth transition between screening factors for negative and positive fields enables estimation of the value in the limit of $E_{\text{ext}} = 0$. The smooth transition is particularly evident for dipolar approximation values, while values arising from the full-multipole approach show more scatter because charge contributions are not confined to a single layer. Screening factor values at $E_{\text{ext}} = 0$ were interpolated using third-order polynomials $-\Delta E_{\text{p}}/E_{\text{ext}} = c_0 + c_1 E_{\text{ext}} + c_2 E_{\text{ext}}^2 + c_3 E_{\text{ext}}^3$ in the interval of field strengths within $\pm 0.5 \text{ V/Å}$, as shown in Figure 4. The bulk screening factor was nearly constant for field strengths lower than 0.4 V/Å , and so it was fitted by a constant function. Fitted points were considered with weights proportional to the inverse square of their uncertainty, which increases for low field strengths due to the factor $1/E_{\text{ext}}$.

Screening factor values in the limit of vanishing external field were used to calculate permittivity values for the full-multipole ($SF^{\text{p}}, \epsilon_r^{\text{p}}$) and dipole moment ($SF^{\text{p1}}, \epsilon_r^{\text{p1}}$) approaches, and are listed in Tables 1 and 2 for the graphite and rutile surfaces. Qualitatively, permittivity varies with distance from interface in

a similar manner for both surfaces (as also observed for SF values), although differences between adjacent water layers are much more pronounced for the rutile surface. Specifically, the negative permittivity of the overscreened contact layer (L1) is followed by the low positive permittivity of the second water layer (L2) due to its reduced screening factor. The dielectric response of L3 closely approaches the overscreening threshold $SF = 1$, which results in large positive or negative permittivities. Note that permittivity diverges to $\pm\infty$ when the dielectric response exactly counterbalances the external field ($SF = 1$) and decays from $-\infty$ to less negative values as the external field becomes overscreened ($SF > 1$). While the differences between L3 permittivity values for dipolar and full-multipole approaches and also between the graphite and rutile surfaces are large, in reality the calculated dielectric responses are similar, as in all cases the external field is nearly exactly canceled out by the dielectric response. Finally, the bulk permittivity values ($\epsilon_r = 58 \pm 3$) are in perfect agreement with literature values for the TIP4P/2005 water model⁵⁵ and are independent of the approach used to calculate the polarization field and surface type.

Beside the results of nonequilibrium simulations, Tables 1 and 2 also contain permittivity values calculated via the fluctuation formula given in eq 10 (ϵ_r^{eq}), and the Kirkwood fluctuation formula ($\epsilon_r^{\text{Kirkwood}}$) given in eq 9. For simplicity, we show only ϵ_r^{eq} from the dipolar approximation, assuming $P = P_1$ in eq 10. The results for ϵ_r^{eq} perfectly match values from nonequilibrium simulations (ϵ_r^{p1}), in agreement with the original studies.^{18,49} However, ϵ_r^{eq} values come from longer simulations ($\sim 15 \text{ ns}$ as compared to $\sim 6 \text{ ns}$ for nonequilibrium

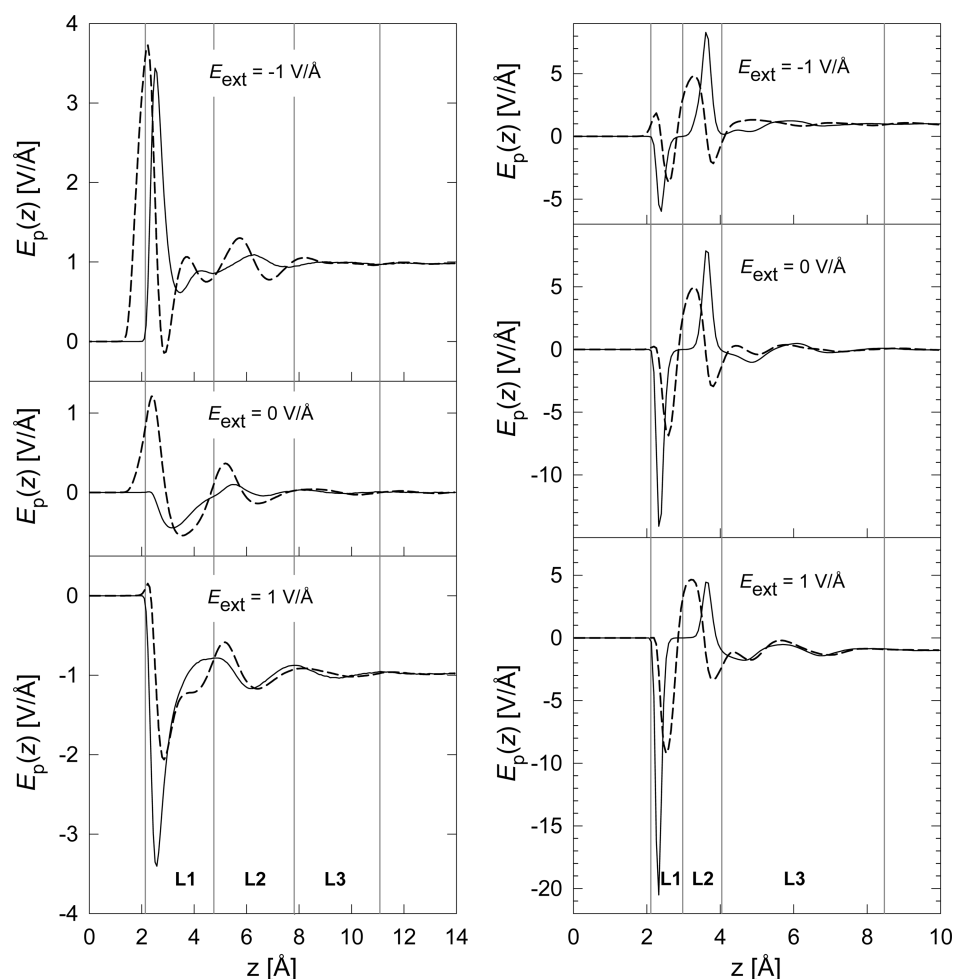


Figure 3. Polarization field of interfacial water at graphite (left) and rutile (right) walls for the external electric fields -1 , 0 , and 1 V/Å. The polarization field generated by dipoles (—) is compared to the full polarization field generated by all multipoles (---). The vertical lines indicate boundaries of the L1, L2, and L3 water layers as defined in Figure 2.

simulations). The slower convergence of the fluctuation formula is illustrated in Figure 5 where profiles of $(\epsilon_r^{P1})^{-1}$ and $(\epsilon_r^{eq})^{-1}$ from ~ 6 ns runs are plotted. The plot is complemented by profiles of $(\epsilon_r^P)^{-1}$ to make a connection between our results for TIP4P/2005 water at hydrophobic graphite and hydrophilic rutile (110) surfaces, with corresponding profiles of SPC/E water at hydrophobic and hydrophilic diamond surfaces shown in Figure 3 of ref 18. The nonequilibrium profiles in Figure 5 were taken from simulations with the weakest external fields applied so as to approach the limit of vanishing external field for which the equilibrium fluctuation formula was derived. Finally, the $\epsilon_r^{\text{Kirkwood}}$ permittivity values fail to reproduce the trends obtained by the other three approaches, and thus should never be used for determination of interfacial permittivity, although such results are frequently published.⁴⁶ Note also that the Kirkwood fluctuation formula yields positive permittivity ex definition.

4.2. Effect of Solvent Molecular Structure on Interfacial Permittivity. Here, we elucidate the molecular-level origins of the interfacial dielectric properties as manifested by strong inhomogeneity and overscreening of the external field, as presented in section 4.1. We start by partitioning the polarization field E_p of an interfacial water layer into the number density ρ and the molecular polarizability, the latter

described by the average z -component value of the individual water dipole moment μ_z :

$$\langle E_p \rangle_{L_i} = -\frac{1}{\epsilon_0} \langle P(z) \rangle_{L_i} = -\frac{1}{\epsilon_0} \langle \rho(z) \rangle_{L_i} \langle \mu_z(z) \rangle_{L_i} \quad (13)$$

For simplicity, we neglect the higher multipoles of polarization density P .

Density variations with the external field are small relative to the polarization field variation (Tables 3 and 4). Therefore, the screening factor can be approximated as

$$\begin{aligned} SF_{L_i} &\equiv -\frac{\Delta \langle E_p \rangle_{L_i}}{E_{\text{ext}}} \\ &\approx \frac{1}{\epsilon_0} \langle \rho(z) \rangle_{L_i} \frac{\Delta \langle \mu_z(z) \rangle_{L_i}}{E_{\text{ext}}} \equiv \frac{1}{\epsilon_0} \langle \rho(z) \rangle_{L_i} \alpha_{L_i} \end{aligned} \quad (14)$$

Thus, the screening factor results from two quantities: density and the response of average molecular dipole moment along the field, referred to as the microscopic or molecular polarizability⁶² $\alpha \equiv \Delta \mu_z / E_{\text{ext}}$. The effect of density on the screening factor is straightforward; if each water dipole changed its orientation by the same amount as in the bulk, the dielectric response and thus the screening factor of a given water layer would be enhanced proportionally to its density. Molecular polarizability accounts for the nonuniform response of the

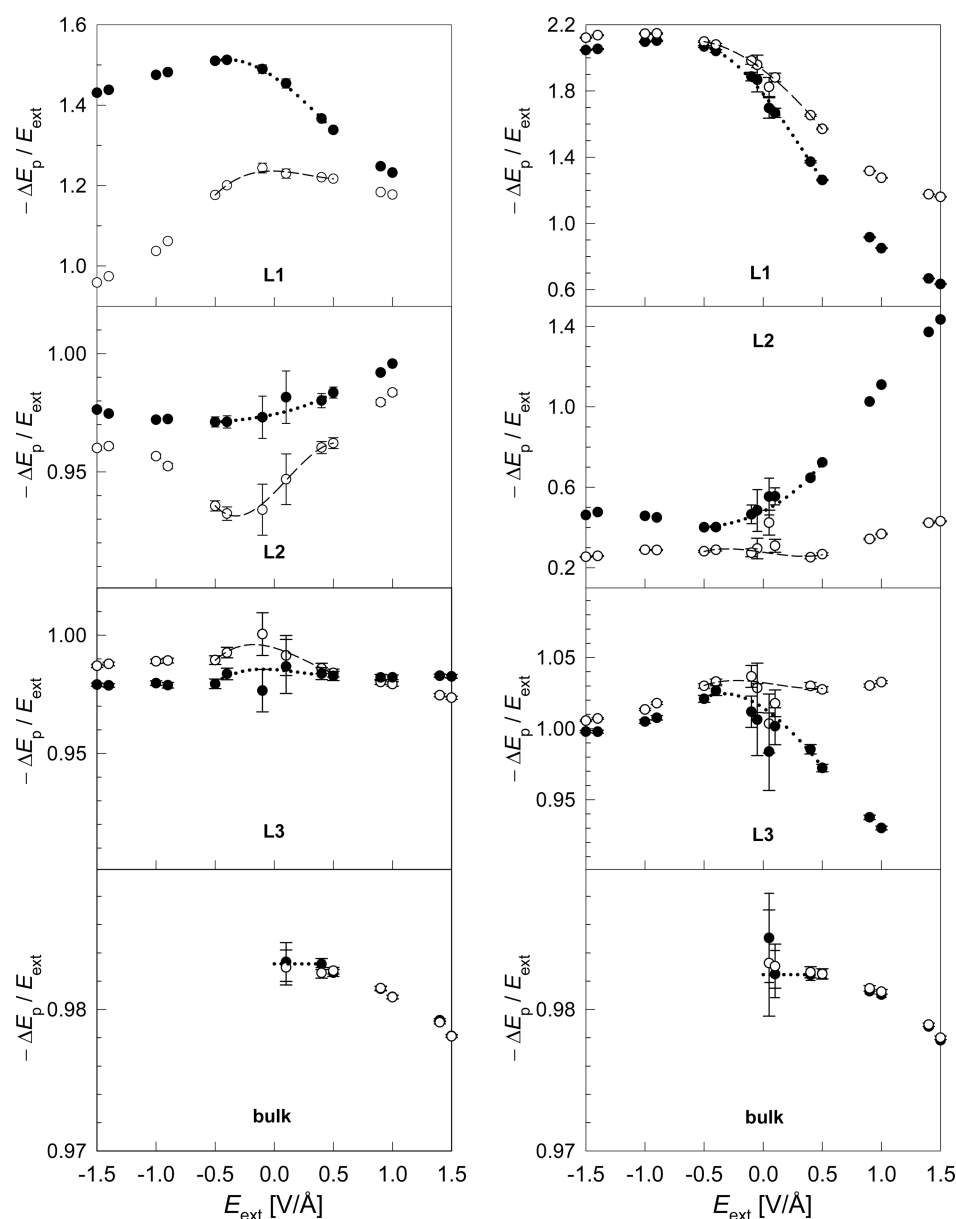


Figure 4. Dielectric screening in terms of the screening factor ($SF = -\Delta E_p/E_{\text{ext}}$) generated by water in the interfacial layers (L1–L3) and in the bulk at graphite (left) and rutile (right) walls. The results based on the dipolar approximation (●) and the full multipole expression (○) are compared. Lines denote polynomial interpolations used to estimate values at $E_{\text{ext}} = 0$.

Table 1. Relative Permittivity of Water in the Interfacial Layers L1–L3 at a Graphite Surface and in the Bulk^a

	graphite surface							
	z_{min} [Å]	z_{max} [Å]	SF^{P}	SF^{P1}	ϵ_r^{P}	ϵ_r^{P1}	ϵ_r^{eq}	$\epsilon_r^{\text{Kirkwood}}$
L1	2.14	4.75	1.23(1)	1.47(1)	−4.2(2)	−2.1(1)	−2.2	75
L2	4.75	7.81	0.94(1)	0.974(5)	17(4)	39(3)	42	44
L3	7.81	11.08	0.995(7)	0.985(7)	187(552)	69(55)	71	42
bulk	15	L-15	0.9828(6)	0.9832(6)	57(2)	60(2)	60	55

^aResults from non-equilibrium simulations using the full-multipole approach (ϵ_r^{P}) and the dipolar approximation (ϵ_r^{P1}), and from equilibrium simulations using the fluctuation formula 10 (ϵ_r^{eq}) and the Kirkwood fluctuation formula 9 ($\epsilon_r^{\text{Kirkwood}}$). Positions of the layers are given by interval ($z_{\text{min}}, z_{\text{max}}$) along the z -axis. The numbers in parentheses indicate the statistical uncertainty in the last digit.

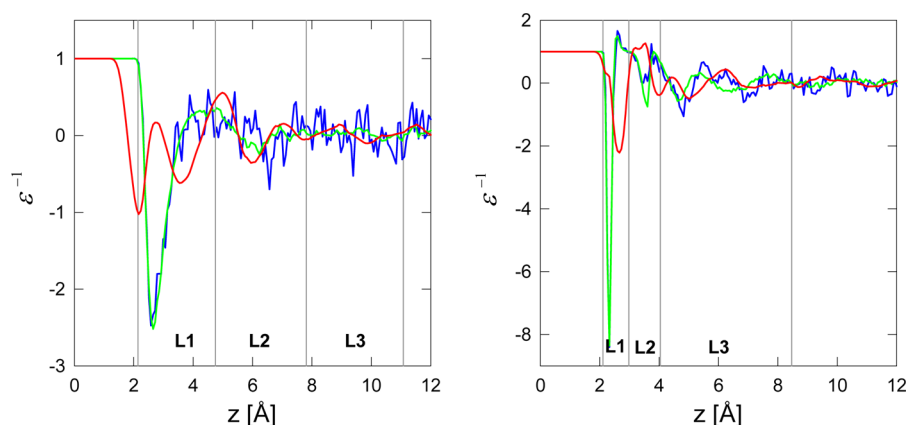
molecular dipole moment because of variable local bonding structure among interfacial water layers, which differs from the bulk value.

Rather than utilizing the field dependence of the average molecular dipole moment, we work with the average cosine of

the angle between the water dipole moment and the surface normal $\langle \mu_z(z) \rangle_{L_i} / \mu$, where $\mu = 0.48 \text{ e} \cdot \text{Å}$ is the magnitude of water dipole moment (for the TIP4P/2005 model). This is convenient because the cosine value can readily be compared to its extreme values of ± 1 , which correspond to the full parallel/

Table 2. Relative Permittivity of Water in the Interfacial Layers L1–L3 at the Rutile (110) Surface and in the Bulk^a

	rutile (110) surface							
	z_{\min} [Å]	z_{\max} [Å]	SF^p	SF^{p1}	ϵ_r^p	ϵ_r^{p1}	ϵ_r^{eq}	$\epsilon_r^{\text{Kirkwood}}$
L1	2.11	2.98	1.93(5)	1.78(5)	−1.08(7)	−1.3(1)	−1.2	33
L2	2.98	4.04	0.29(5)	0.48(3)	1.4 (1)	1.9(1)	1.8	59
L3	4.04	8.47	1.03(1)	1.02(1)	−31(14)	−69(80)	−31	49
bulk	15	L-15	0.9825(5)	0.9825(6)	57(2)	57(2)	58	58

^aFootnotes are the same as those in Table 1.Figure 5. Inverse permittivity of water at graphite (left) and rutile (right) surfaces calculated from the full-multipole approach $(\epsilon_r^p)^{-1}$ (red) and from the dipole moment approximation using nonequilibrium simulations $(\epsilon_r^{p1})^{-1}$ (green) or the equilibrium fluctuation formula $(\epsilon_r^{eq})^{-1}$ (blue). Results are from simulation runs of the same length (~ 6 ns).Table 3. Dielectric Properties of Water at the Graphite Surface: Polarization Field E_p , Mass Density ρ_m , and Average Cosine of the Angle between Water Dipoles and the Surface Normal μ_z/μ in the Interfacial Layers L1–L3, and in the Bulk for Selected External Field Strengths^a

	E_{ext} [V/Å]								
	−1.5	−1	−0.5	−0.1	0	0.1	0.5	1	1.5
	$E_p = -P_1/\epsilon_0$ [V/Å]								
L1	1.913	1.242	0.522	−0.084	−0.233	−0.378	−0.902	−1.465	<i>b</i>
L2	1.476	0.983	0.497	0.108	0.011	−0.087	−0.481	−0.985	<i>b</i>
L3	1.473	0.984	0.494	0.102	0.005	−0.094	−0.486	−0.977	−1.469
bulk					0.000	−0.098	−0.491	−0.981	−1.467
	ρ_m [g/cm ³]								
L1	1.24	1.16	1.08	1.09	1.10	1.11	1.15	1.20	<i>b</i>
L2	1.00	0.98	1.00	1.02	1.02	1.02	1.02	1.01	<i>b</i>
L3	1.00	0.99	1.00	1.00	1.00	1.00	1.00	0.99	1.00
bulk					1.00	1.00	1.00	0.99	1.00
	μ_z/μ								
L1	−0.530	−0.368	−0.166	0.027	0.073	0.117	0.270	0.419	<i>b</i>
L2	−0.506	−0.343	−0.171	−0.037	−0.004	0.029	0.162	0.336	<i>b</i>
L3	−0.507	−0.342	−0.171	−0.035	−0.002	0.032	0.168	0.339	0.505
bulk					0.000	0.034	0.169	0.340	0.506

^aThe screening factor SF , cf., eq 8 and Figures 4 and 6, is calculated by subtraction of the polarization field in a column for a given E_{ext} and in the central column for $E_{\text{ext}} = 0$. ^bData were not analyzed due to significant modification of the density profiles and layer boundaries.

antiparallel alignment of dipoles. The average cosine is plotted in Figure 6 (relative to the right vertical axes) together with the screening factor (as in Figure 4 but with a uniform vertical scale). Molecular polarizability at a given E_{ext} can be inferred from this figure as the slope of the secant line between the average cosine value at E_{ext} and 0. A concave/linear/convex shape to the cosine dependence corresponds to a decreasing/constant/increasing molecular polarizability α , and, according to eq 14, also to a decreasing/constant/increasing screening factor. The truly linear dependence of the dipole cosine,

corresponding to a constant α , is inherently present at small external fields for the bulk phase where no influence of surface interaction persists. Closer to the interface, particularly in L1 and L2, the local bonding network affects water dipole orientation, producing a nonzero polarization ($\mu_z/\mu \neq 0$) at zero external field and altering the dipole cosine dependence differently as compared to the bulk. Specifically, the alignment of L1 dipoles in the direction of the zero-field polarization (along the positive z -axis) is hindered as compared to reorientation in the opposite direction. As a result, α decreases

Table 4. Dielectric Properties of Water at the Rutile (110) Surface^a

	$E_{\text{ext}} [\text{V/\AA}]$								
	−1.5	−1	−0.5	−0.1	0	0.1	0.5	1	1.5
	$E_p = -P_1/\epsilon_0 [\text{V/\AA}]$								
L1	−0.871	−1.844	−2.907	−3.752	−3.941	−4.107	−4.572	−4.791	−4.892
L2	2.891	2.656	2.399	2.245	2.199	2.145	1.839	1.091	0.050
L3	1.359	0.867	0.373	−0.036	−0.141	−0.246	−0.632	−1.076	<i>b</i>
bulk					0.000	−0.098	−0.491	−0.981	−1.467
	$\rho_m [\text{g/cm}^3]$								
L1	1.78	1.78	1.78	1.78	1.78	1.78	1.78	1.78	1.78
L2	1.45	1.45	1.45	1.46	1.46	1.46	1.46	1.44	1.37
L3	0.95	0.94	0.94	0.94	0.94	0.95	0.95	0.97	<i>b</i>
bulk					1.00	1.00	1.00	1.00	1.00
	μ_z/μ								
L1	0.169	0.357	0.562	0.725	0.762	0.794	0.884	0.926	0.945
L2	−0.685	−0.630	−0.569	−0.531	−0.519	−0.506	−0.433	−0.261	−0.013
L3	−0.495	−0.319	−0.137	0.013	0.053	0.089	0.228	0.383	<i>b</i>
bulk					0.000	0.034	0.169	0.340	0.506

^aFootnotes are the same as those in Table 3.

markedly for positive external fields and, equivalently, SF decreases more steeply on the positive branch of external fields. In the case of the rutile surface, the decrease of SF in L1 for positive fields is enhanced due to saturation of the dipole cosine when close to its maximum value +1. This decrease is balanced by a comparable increase in L2, where the external field is poorly screened by L1, whereas for negative and low positive external fields α is low, resulting in low SF . The same effect is also noticeable at the graphite interface, although it is much less pronounced (see the detailed dependence of the screening factor in Figure 4). The mild interaction of the graphite surface with interfacial water layers is reflected by the roughly linear dependence of the average cosine with substantial deviations only in L1. In addition, the zero field cosine is small in all interfacial water layers, in agreement with previous findings that water molecules orient primarily parallel to the graphite surface.⁶³ On the other hand, the influence of rutile–water interactions persists markedly in all interfacial water layers as manifested by the series of oppositely oriented dipole moments: $\mu_z/\mu = 0.76$, -0.52 , and 0.05 in L1, L2, and L3, respectively, for $E_{\text{ext}} = 0$.

In the previous paragraph, the dependence of the average cosine of the interfacial water layers was discussed for the entire range of applied fields. However, for the determination of permittivity at experimentally relevant conditions, only the slope of the dependence around $E_{\text{ext}} = 0$ is important. In Figure 7, a comparison of the slopes, that is, molecular polarizabilities $\alpha_{L,i}$ at $E_{\text{ext}} = 0$ in the three water layers as well as the bulk is given. For the graphite interface, only the molecular polarizability of L1 differs markedly from the bulk value, while for the rutile interface, L2 and L3 exhibit deviating molecular polarizability (slightly increased in L3, and significantly reduced in L2). The ratios of layer susceptibilities to the bulk are given in Table 5. Given that the density ratios are $\langle\rho\rangle_{L1}:\langle\rho\rangle_{L2}:\langle\rho\rangle_{L3}:\langle\rho\rangle_{\text{bulk}} = 1.10:1.02:1.00:1.00$ for graphite, and $1.78:1.46:0.94:1.00$ for rutile interfaces, the consequences of eq 14 for screening factors and permittivities are as follows. For the graphite interface, the screening factor is a combined effect of density and molecular polarizability. For the rutile interface, the overscreening of L1 is a direct consequence of the increased density, while the poor screening of L2 and the slight overscreening of L3 arise solely from a reduced and slightly

enhanced molecular polarizability, respectively. Although the dielectric profile at the two interfaces is qualitatively the same, that is, an overscreening response ($SF > 1$, negative permittivity) for L1, a reduced response ($SF < SF_{\text{bulk}}$, low positive permittivity) for L2, and a slightly enhanced response for L3 ($SF \geq SF_{\text{bulk}}$, singular permittivity), we can now see that the mechanisms underlying the dielectric response are different.

So far, the dielectric response has been described rather phenomenologically. In the following, we elucidate how molecular polarizability arises from the local bonding network. Molecular polarizability α reflects the ease of alignment of a molecular dipole along an applied field. On a molecular scale, polarizability depends on the local mean force acting on a molecule toward an applied field, which arises from the distortion of an equilibrium bonding network. In Tables 6 and 7, the number of bonds between the studied structural layers and their energy are given. Bonds are defined to form between oppositely charged sites of different molecules, which includes water–water hydrogen bonds and bonds with surface groups in the case of rutile: hydrogen bonds between water hydrogen and BO and between water oxygen and Ti. Bonds were identified on the basis of a geometric criterion; that is, a bond exists when the interaction sites are closer than a maximum bond length r_{max} defined as the position of the first minimum in the corresponding site–site radial distribution function. The bond characteristics are surveyed in Table 8, and bonds are visualized in Figure 8. The energy of bonds was sampled directly in the simulation, together with calculation of forces between interacting sites.

For the graphite surface (Table 6), the energy (strength) of hydrogen bonds between various structural layers is similar. Hence, the resistance of a water molecule to reorientation is related to the number of bonds the molecule forms (coordination number). Comparison of the number of bonds per molecule in the layers L1–L3 with corresponding molecular polarizability from Table 5 (and Figure 7) confirms that the enhanced molecular polarizability of L1 is caused by the reduced number of bonds, which eases the alignment of molecular dipoles in an applied field relative to the bulk. The coordination number in subsequent layers is similar to the bulk value with a slightly increased value in L2, again in line with the reduced molecular polarizability.

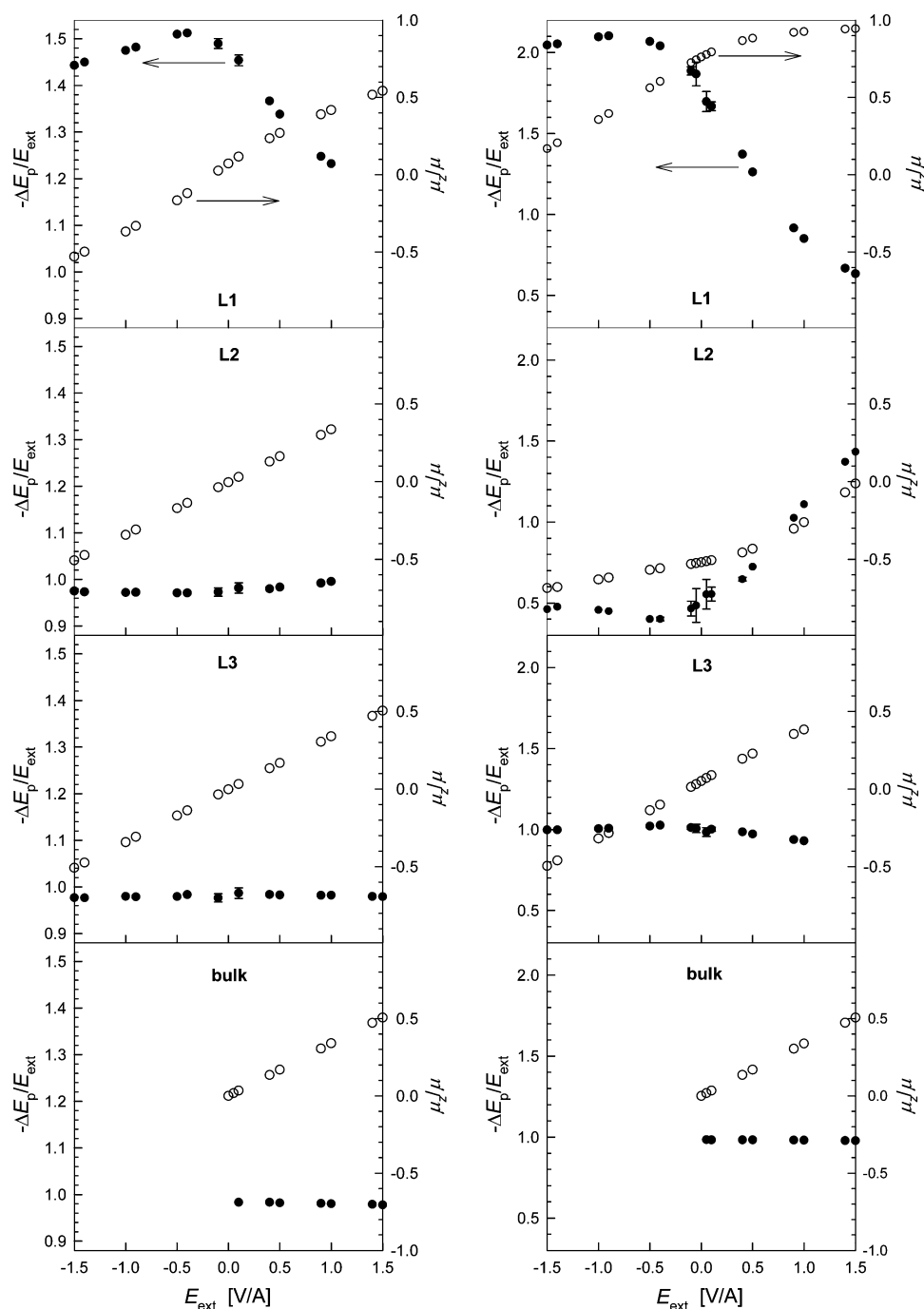


Figure 6. Screening factor (SF) (●, left vertical axes) and average cosine of the angle between water molecule dipole moment and the surface normal (○, right vertical axes) in the interfacial water layers (L1–L3) and in bulk water for graphite (left) and rutile (right) surfaces.

In the case of the rutile surface (Table 7), the bonding network is more complex as strong bonds with the surface exist. Hence, the number of bonds has to be analyzed together with their strength. Although the number of bonds per molecule in L1 is lower than in bulk, their strength limits the alignment of a L1 water molecule, so that the resulting molecular polarizability is the same as for the bulk (this similarity is coincidental). The dense bonding network around L2 water molecules (our simple definition of a bond allows “overbonding”, i.e., number of bonds per water molecule >4) is supported by high bonding strength, which together are responsible for the low α . For L3, the increased α seems to be a prevailing effect of a reduced

bond strength rather than a slightly increased coordination number.

4.3. Electrostatic Profile at Charged Surfaces and Capacitance of the Stern Layer. In this section, we will link MD simulation results to the surface complexation modeling of macroscopic experimental data. To study EDL structure, a simulation of electrolyte contacting a charged rutile surface was carried out, and the electrostatic profile was analyzed. Next, the capacitance of the Stern layer, which is one of the key surface complexation variables, will be determined using the permittivity profile of water determined in section 4.1.

Simulation of the negatively charged rutile (110) surface was carried out by adding hydroxyl groups to terminal Ti atoms and

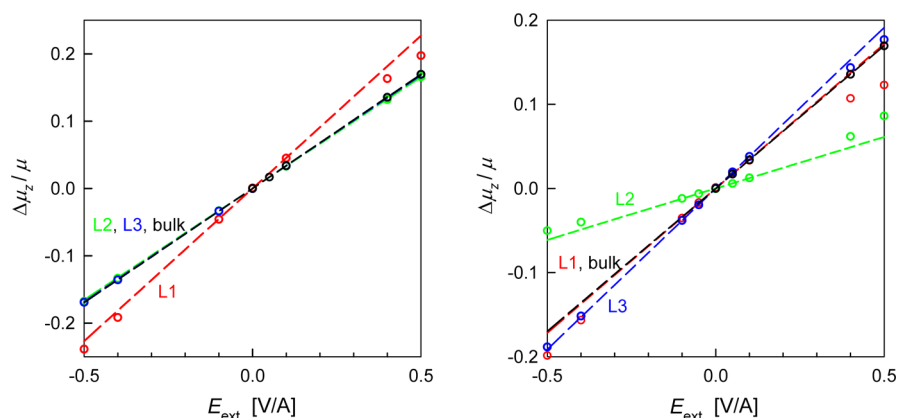


Figure 7. Response of a water molecule's dipole orientation to the applied field in the interfacial water layers L1 (red), L2 (green), L3 (blue) and in bulk (black) for graphite (left) and rutile (right) interfaces. Simulation data, taken from Figure 6, were fitted by linear function $a \cdot E_{\text{ext}}$ in the interval $E_{\text{ext}} \in [-0.1, 0.1]$ V/Å. The slope $a = \alpha/\mu$ yields molecular polarizability α .

Table 5. Density, Molecular Polarizability, and Screening Factor (SF^{P1}) of the Interfacial Water Layers L1–L3 Normalized by the Bulk Values^a

	graphite			rutile		
	$\rho_{\text{Li}}/\rho_{\text{bulk}}$	$\alpha_{\text{Li}}/\alpha_{\text{bulk}}$	$SF_{\text{Li}}/SF_{\text{bulk}}$	$\rho_{\text{Li}}/\rho_{\text{bulk}}$	$\alpha_{\text{Li}}/\alpha_{\text{bulk}}$	$SF_{\text{Li}}/SF_{\text{bulk}}$
L1	1.10	1.34	1.495	1.78	1.01	1.812
L2	1.02	0.98	0.991	1.46	0.36	0.489
L3	1.00	1.00	1.002	0.94	1.13	1.038

^aThe normalized values of density and molecular polarizability represent their effect on the resulting screening factor, cf., eq 14.

Table 6. Number and Energy of Hydrogen Bonds between Structural Layers at the Graphite Surface^a

	no. of bonds					bonds/ molecule
	L1	L2	L3	rest	bulk	
L1	633.3	240.0				3.30
L2		591.7	240.7			3.74
L3			634.6	242.6		3.71
rest				4069.5	242.9	3.71
bulk					3177.3	3.71
	bond energy [kJ/mol]					average
	L1	L2	L3	rest	bulk	
L1	−19.3	−18.7				−19.1
L2		−18.9	−18.8			−18.8
L3			−19.0	−18.9		−18.9
rest				−18.9	−18.9	−18.9
bulk					−18.9	−18.9

^aThe number of bonds per molecule, a measure of its resistance to reorientation, explains molecular polarizability α given in Table 5: the higher is the number of bonds per molecule, the lower is the molecular polarizability. Structural layers are defined as in Table 1 with “rest” being a region residing between L3 and bulk. The absolute number of bonds refers to the number of water molecules in the unit simulation cell (265, 287, 301, 1227, and 921 molecules in L1, L2, L3, rest, and bulk, respectively).

redistributing their charge over the surface as described in ref 10. The total surface charge density was ~ -0.1 C/m² and was neutralized by excess Na⁺ ions of the background NaCl electrolyte (0.35 M). The electrostatic potential profile and cumulative charge density are given in Figure 9. The

electrostatic potential ψ was calculated by the following equation:

$$\psi(z) = -\frac{1}{\epsilon_0} \int_{-\infty}^z dz' \rho_q(z')(z - z') \quad (15)$$

Hence, both quantities stem from the charge density ρ_q , which can be decomposed into contributions from surface atoms, ions, and water. In Figure 9, the full profiles (solid lines), the profiles generated by the ions plus the surface charge (dashed lines), and those generated by pure water at the neutral rutile surface (dotted lines) are shown. Interestingly, the rapid oscillations of the full potential profile at the charged surface are nicely matched by the profile for pure water at the neutral surface. Comparison of the two profiles derived from electrolyte solution reveals that the slowly decaying ions + surface potential is largely compensated by the water contribution, which causes the full potential to be much more short ranged. This is further evidence, in addition to studies of interfacial diffusivity¹⁵ and viscosity,¹⁶ that the effective range of surface–solution or solute–solvent interactions in aqueous solutions is only about 15 Å, in contrast to theories based on implicit solvent models that predict an effective surface interaction range (such as the position of the “shear plane”) of several nanometers, depending on the ionic strength. The dissimilarity between full electrostatic profile and that generated by ions + surface charge shows that water dielectric properties cannot be described accurately by simple models, which neglect its molecular structure. The cumulative charge density reveals that the surface charge is overscreened by the ionic charge beyond the adsorption plane of cations (~ 3.5 Å). This phenomenon has been observed previously for both hydrophilic and hydrophobic surfaces.⁶⁴ Throughout this Article, the term “overscreening” refers to the total electric field response having a different sign than the external field. In a broader sense, which covers the case of solutions containing ions, the external field can be considered as generated by charge density excluding the solvent contribution, that is, $E_{\text{ext}} = \frac{1}{\epsilon_0} \int_{-\infty}^z dz' \rho_{q,\text{ions+surface}}(z') = \frac{D}{\epsilon_0}$. From this, “overscreening” can be defined as the total electric field response ΔE having a sign opposite to the displacement field, D/ϵ_0 . The dashed line in Figure 9 (bottom) is equal to the displacement field D , and the difference between the full (solid) and neutral surface (dotted) profiles is equal to $\Delta \int_{-\infty}^z dz' \rho_q(z') = \frac{\Delta E}{\epsilon_0}$.

Table 7. Number and Energy of Bonds between Structural Layers at the Rutile (110) Surface^a

	no. of bonds						bonds/molecule
	surface	L1	L2	L3	rest	bulk	
L1	173.0	123.3	117.2	82.9			3.45
L2	142.9		178.9	166.3			4.17
L3				941.6	244.7		3.73
rest					4735.7	242.6	3.71
bulk						3173.2	3.71
	bond energy [kJ/mol]						average
	surface	L1	L2	L3	rest	bulk	
L1	−69.1	−7.5	−18.2	−16.8			−33.0
L2	−41.5		−14.1	−18.3			−22.5
L3				−18.8	−18.8		−18.7
rest					−18.9	−18.9	−18.9
bulk						−18.9	−18.9

^aThe number of bonds per molecule and their energy govern resistance of a molecule to reorientation, and can be used to account for the molecular polarizability α given in Table 5. Structural layers are defined as in Table 2 with “rest” being a region residing between L3 and bulk. The absolute number of bonds refers to the number of water molecules in the unit simulation cell (144, 145, 385, 1406, and 920 molecules in L1, L2, L3, rest, and bulk, respectively).

Table 8. Bonds Are Defined To Form between Oppositely Charged Sites Distanced Less than r_{\max} ^a

bond type	r_{\max} [Å]
HW–OW	2.43
HW–BO	2.43
OW–Ti	3.23

^aHydrogen bonds form between the positive (HW) and negative (OW) sites on different water molecules; bonds with the rutile (110) surface involve bridging oxygen (BO) or terminal titanium (Ti).

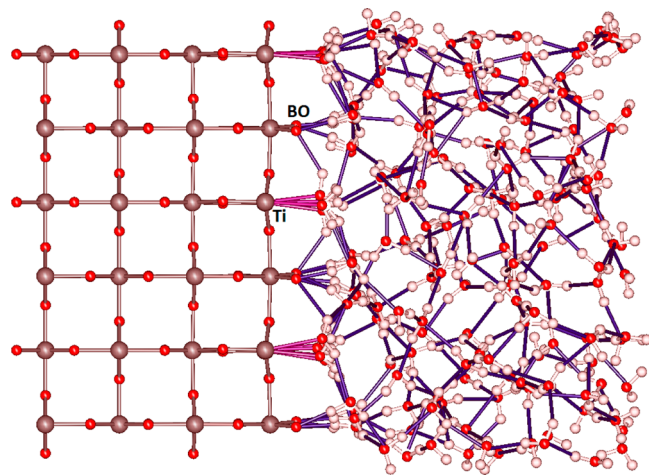


Figure 8. Bonding network at the rutile (110)–water interface. Hydrogen bonds between water molecules and those with bridging oxygens (BO) of the surface are shown in blue, while bonds with surface titanium atoms (Ti) are magenta. The figure covers the same region as in Figure 1.

Therefore, it can be seen that the region of overscreening (in the above-defined sense) does not coincide with the region of overscreening of the surface charge by the ionic charge. Therefore, the two different overscreening phenomena are not directly related.

The electrostatic profile at a charged surface gives rise to capacitance. It is tempting to calculate capacitance directly from Figure 9 as the quotient of surface charge density σ_0 over surface potential Ψ_0 . Note, however, that a nontrivial surface

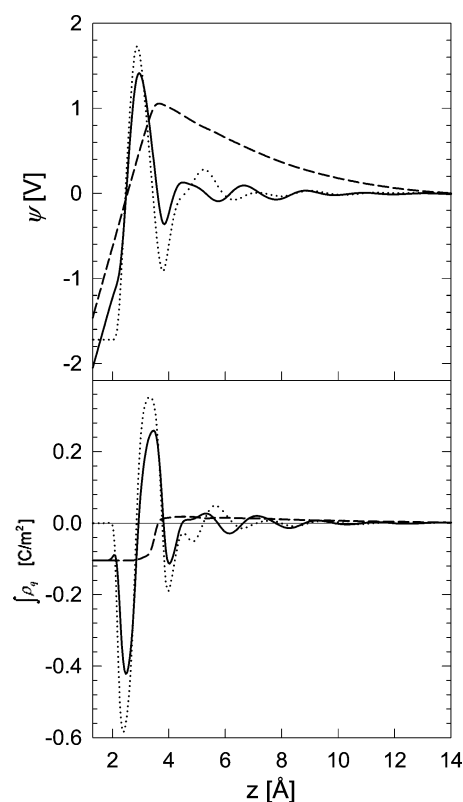


Figure 9. Electrostatic potential (top) and cumulative charge density (bottom) of 0.35 M NaCl electrolyte in contact with a negatively charged rutile (110) surface of surface charge density ≈ -0.1 C/m². The full profiles (—) are compared to those due to the distribution of ions (---), that is, lacking the contribution of water, and to distributions for pure water at a neutral (for $E_{\text{ext}} = 0$) rutile surface (...).

potential exists even for a neutral surface due to the interfacial structure of water (dotted line, Figure 9 (top)). Following the discussion of the derivation of interfacial permittivity, the capacitance value that can be linked to experimental data is

$$c = \frac{\Delta\sigma_0}{\Delta\psi_0} \quad \text{or} \quad c = \frac{d\sigma_0}{d\psi_0} \quad (16)$$

Calculation of capacitance according to eq 16 directly from simulation would require having a consistent molecular model for a variable charged surface. Here, we calculate capacitance from the permittivity of water, as determined in section 4.1, exploiting the following chain of equations:

$$c = \frac{\Delta\sigma_0}{\Delta\psi_0} = \frac{\Delta\sigma_0}{\Delta \int E dz} \approx \frac{\epsilon_0 \Delta\sigma_0}{\int \epsilon_r^{-1} \Delta D dz} \approx \frac{\epsilon_0}{\int \epsilon_r^{-1} dz} \quad (17)$$

where we assume that presence of ions does not affect solvent permittivity and that changing the surface charge (at constant number of ions) does not affect ionic distribution, so that $\Delta D(z) = \Delta\sigma_0$. Neglecting the impact of ions on permittivity implies the capacitance is independent of electrolyte type and ionic strength. Such an approximation is also widely used in surface complexation modeling where various EDL models are fit to experimental surface titration data for various electrolytes and ionic strengths to arrive at a unique capacitance value for each Stern layer included.^{29,35} The other approximation, $\Delta D(z) = \Delta\sigma_0$, is reasonable when the change in cumulative ionic charge distribution is small as compared to added surface charge, $\int_{-\infty}^z dz' \Delta\rho_{q,ions}(z') < \Delta\sigma_0$. The change in $\Delta\rho_q$ is sometimes substantial, for example, Na^+ moving from a bidentate to a tetradentate binding mode with increasing negative surface charge.⁶⁴ Nevertheless, these changes might be counterbalanced when integrated over the Stern layer, which we are interested in. In addition to the discussed assumptions, the local relation between the electric and displacement fields, $D(z) = \epsilon_r(z)\epsilon_0 E(z)$, was used, which is justified provided the displacement field varies much slower than the electric field, as evident from Figure 9 (bottom).

The Stern layer capacitance is defined as

$$c_s = \frac{\Delta\sigma_0}{\Delta(\psi_0 - \psi_s)} \approx \frac{\epsilon_0}{\int_{z_0}^{z_s} \epsilon_r^{-1} dz} \quad (18)$$

where Ψ_s is the electrostatic potential at the Stern plane located at distance z_s from the surface. In surface complexation modeling, c_s plays the key role as a general characteristic of the solid–solution interface. Ridley et al.⁶⁵ fit experimental titration data for rutile in several 1–1 electrolytes at ambient conditions with the basic Stern model, and the resulting Stern layer capacitance was about 0.6 F/m². Here, we calculated the capacitance according to eq 18 using the permittivity profile ϵ_r^p shown in Figure 5 with the inverse permittivity integrated between the surface charge and Stern planes. The Stern plane position at $z_s = 3.5$ Å was inferred from Figure 9 assuming that it coincides with the peak position of Na^+ counterions. However, the position of the surface charge plane z_0 is more ambiguous and does not necessarily coincide with $z = 0$, defined as the position of interfacial Ti atoms (see Figure 1) because bridging oxygen atoms (BO) and terminal hydroxyl groups (TOH) also carry charge. These BO and TOH groups are located 1.14 and 1.87 Å above the Ti atom surface plane, respectively. The running integral $\int_0^z \epsilon_r^{-1}(z') dz'$ is plotted in Figure 10, and the value of the integral between boundaries a (z_0) and b (z_s) is given as a difference between the values on the curve at b and a . The effect of varying the integration boundaries on the capacitance is shown in the inset where the

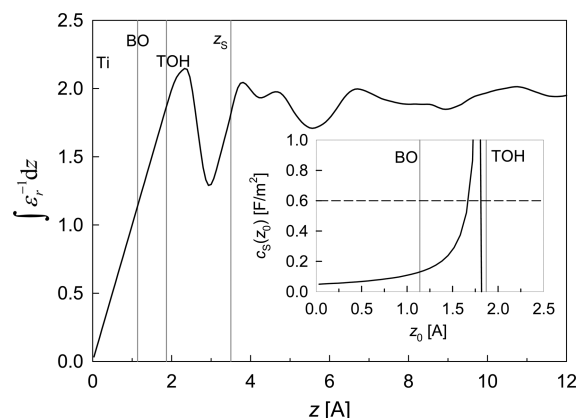


Figure 10. Running integral of inverse permittivity ϵ_r^p taken from Figure 5. The positions of surface groups are indicated by vertical lines: Ti = interfacial titanium atoms, BO = bridging oxygen, TOH = oxygen of hydroxyl group of a negatively charged rutile surface. The effect of position of the surface charge plane z_0 on the Stern layer capacitance c_s is shown in the inset. The dashed line indicates the value obtained by surface complexation modeling of experimental rutile titration data as presented in ref 65.

upper boundary is fixed at $z_s = 3.5$ Å, while the lower boundary varies between $z_0 = 0$ (position of Ti) and $z_0 = 1.87$ Å (position of TOH). The calculated capacitance strongly depends on the chosen position of the surface charge plane, and it increases as $1/(z - z_0)$ when approaching $z_0 = 1.83$ Å (just before the position of TOH). At that position, the integral in eq 18 vanishes, and the calculated capacitance is negative at greater distances because of the dominant influence of the L1 water layer, which has negative permittivity. However, negative capacitances have never been observed experimentally, which suggests that the negative permittivity (if it exists at all; note that ionization effects and electronic polarizability are neglected in our molecular models) is compensated by the positive permittivity of the depletion layer (between the surface and water) where $\epsilon_r^{-1} = 1$. The value of $c_s = 0.6$ F/m², determined by surface complexation modeling, corresponds to $z_0 = 1.7$ Å, that is, between the BO and TOH surface groups. This is reasonable because both groups carry charge and participate in binding ionic species. Moreover, most solid surfaces are not perfectly planar and are populated by charged surface groups at different heights, so locating the surface charge plane (z_0) will often be ambiguous.

4.4. Significance of Solvent Molecular Structure. Our results of the distance-dependent permittivity at a solid–liquid interface are in contrast with the implicit solvent model picture, where the relative permittivity of interfacial water typically decreases monotonically toward the surface from bulk values to low positive values at the interface.^{26,27,29,31,37,38} A critical shortcoming of implicit solvent models is that they account for interfacial dielectric properties with the same relations used for homogeneous systems. Consequently, the permittivity of interfacial water is lower than in bulk due to saturation of the water dipoles according to a relation between field strength and permittivity of a homogeneous continuum, such as the Booth relation:^{31,66,67}

$$\epsilon_r(E) = n^2 + (\epsilon_r(0) - n^2) \frac{3}{bE} \left[\coth(bE) - \frac{1}{bE} \right],$$

$$b = \frac{\sqrt{73}}{6} (n^2 + 2) \beta \mu \quad (19)$$

where n is the refractive index. In contrast, our results reveal that the dielectric responses of interfacial and bulk water molecules to an external field are different (see Figures 4 and 6).

This discrepancy arises because implicit solvent models do not consider spatial variations in solvent structure. For example, eq 19 only accounts for a permittivity decrease from saturation of the dielectric response when dipoles are aligned with the field. However, our simulation results demonstrate that variations in density and molecular polarizability due to the presence of surfaces also have a significant effect on the dielectric response. For the strongly hydrophilic rutile surface, these surface-induced variations increase (in L1) or decrease (in L2) the dielectric response by a factor of 2 relative to the bulk response. A similar effect is evident also for the weakly interacting graphite surface where the locally decreased molecular polarizability (and increased density), resulting from the lack of bonding partners, leads to a dielectric response (of L1) enhanced by a factor 1.5 relative to bulk water. In both cases, the effect of interfacial water structure leads to overscreening of the external field by the dielectric response, a phenomena that does not occur in bulk water at any field strength and therefore cannot be described by bulk relations, such as eq 19.

This has an important implication for theoretical models of interfaces: if density and molecular polarizability variations of the solvent are significant enough to cause overscreening of the external field, then the solvent contribution to the electrostatic potential profile and other interfacial dielectric properties can no longer be considered as secondary to ionic contributions. As shown in Figure 9, the structure of water molecules actively forms and dominates the electrostatic profile rather than diminishing the electric field radiated by the rutile (110) surface and ions.

5. CONCLUSIONS

We applied nonequilibrium molecular simulations to study the dielectric response of interfacial water perturbed by external electric fields normal to the interface. Analysis of water layers at weakly interacting (hydrophobic) graphite and strongly interacting (hydrophilic) rutile (110) surfaces revealed the effect of solvent molecular structure induced by the surface on dielectric properties, which is neglected in implicit solvent models. The key findings can be summarized as follows.

- (a) The dependence of the dielectric response on the external field in the interfacial region differs entirely from the response in bulk (homogeneous) water, leading to strong deviations in permittivity. A particularly strong and weak dielectric response was found in the contact and second hydration layer, respectively.
- (b) The dielectric response was found to arise from local density and molecular polarizability, that is, the response in orientation of an individual molecule. The interplay between both factors means that that preferential alignment of dipoles does not necessarily lead to a reduced dielectric response as commonly assumed on the basis of bulk behavior. On the contrary, an enhanced or even an overscreening response, leading to negative permittivity, can occur in a local part of the system, particularly at the interface, where multiple interactions interplay. The permittivity of a macroscopic continuous system must be larger than unity in accordance with

stability laws; however, negative permittivity in a finite part of an inhomogeneous system does not violate these laws. Moreover, such localized phenomena cannot be accounted for by the bulk-like relations used in implicit solvent models.

- (c) The molecular level origin of the dielectric response resides in the solvent structure determined by the local density and H-bonding network. Molecular polarizability shows a negative correlation with number of bonds per molecule and bond strength.
- (d) The interfacial dielectric properties are qualitatively similar for both the graphite (hydrophobic) and the rutile (110) (hydrophilic) surfaces, although the underlying mechanisms are a bit different. The overscreening response of the contact layer is an effect of augmented density at the rutile surface, while it results more from increased molecular polarizability due to the lack of H-bonding partners at the graphite surface. The limited molecular polarizability of the densely bonded second water layer is responsible for its reduced response and low permittivity at both surfaces, but especially for rutile.
- (e) The equilibrium fluctuation formulas of Ballenegger et al.⁴⁹ and Bonhuis et al.¹⁸ yield excellent agreement with the nonequilibrium approach using an external field. On the other hand, the Kirkwood fluctuation formula, which was derived for homogeneous isotropic fluids, should not be used to calculate interfacial permittivities.
- (f) The results obtained for neutral surfaces in contact with pure water were compared to a simulation of a negatively charged rutile surface interacting with 0.35 M NaCl. The corresponding electrostatic potential profiles were very similar, which supports the “water centric” as opposed to the “ionic centric” concept of electrical double layers, as the dominant contribution comes from the charge density distribution of water.
- (g) The calculated permittivity profile at the rutile (110) surface yields a Stern layer capacitance value compatible with that obtained from surface complexation modeling of experimental titration data provided the surface charge plane is set to reside between the two charged surface groups, which reside at different heights. The ambiguity in setting the location of the surface charge plane for atomically rough surfaces is the main limitation in predicting the capacitance of interfacial layers from computer simulations.

Future studies toward a better understanding of interfacial dielectric properties should address the impact of ions on permittivity and utilize polarizable simulation models.

AUTHOR INFORMATION

Corresponding Author

*E-mail: parez@icpf.cas.cz.

Notes

The authors declare no competing financial interest.

ACKNOWLEDGMENTS

This research was supported by the Czech Science Foundation (project nos. 13-08651S and 13-09914S). Access to the MetaCentrum computing facilities, provided under the programme “Projects of Large Infrastructure for Research, Development, and Innovations” LM2010005 funded by the Ministry of Education, Youth, and Sports of the Czech

Republic, is acknowledged. M.M. was supported by the U.S. Department of Energy, Office of Science, Basic Energy Sciences, Chemical Sciences, Geosciences, and Biosciences Division, to help interpret the MD results and relate them to macroscopic data.

REFERENCES

- (1) Kavathekar, R. S.; Dev, P.; English, N. J.; MacElroy, J. M. D. Molecular Dynamics Study of Water in Contact with the TiO₂ Rutile-110, 100, 101, 001 and Anatase-101, 001 Surface. *Mol. Phys.* **2011**, *109*, 1649–1656.
- (2) Koparde, V. N.; Cummings, P. T. Molecular Dynamics Study of Water Adsorption on TiO₂ Nanoparticles. *J. Phys. Chem. C* **2007**, *111*, 6920–6926.
- (3) Wang, J.; Kalinichev, A. G.; Kirkpatrick, R. J. Effects of Substrate Structure and Composition on the Structure, Dynamics, and Energetics of Water at Mineral Surfaces: A Molecular Dynamics Modeling Study. *Geochim. Cosmochim. Acta* **2006**, *70*, 562–582.
- (4) Wolthers, M.; Di Tommaso, D.; Du, Z.; de Leeuw, N. H. Calcite Surface Structure and Reactivity: Molecular Dynamics Simulations and Macroscopic Surface Modelling of the Calcite-Water Interface. *Phys. Chem. Chem. Phys.* **2012**, *14*, 15145–15157.
- (5) Philpott, M. R.; Goliney, I. Y.; Lin, T. T. Molecular Dynamics Simulation of Water in a Contact with an Iron Pyrite FeS₂ Surface. *J. Chem. Phys.* **2004**, *120*, 1943–1950.
- (6) Tournassat, C.; Chapron, Y.; Leroy, P.; Bizi, M.; Boulahya, F. Comparison of Molecular Dynamics Simulations with Triple Layer and Modified Gouy-Chapman Models in a 0.1M NaCl-Montmorillonite System. *J. Colloid Interface Sci.* **2009**, *339*, 533–541.
- (7) Bourg, I. C.; Sposito, G. Molecular Dynamics Simulations of the Electrical Double Layer on Smectite Surfaces Contacting Concentrated Mixed Electrolyte (NaCl-CaCl₂) Solutions. *J. Colloid Interface Sci.* **2011**, *360*, 701–715.
- (8) Rosenqvist, J.; Machesky, M. L.; Vlcek, L.; Cummings, P. T.; Wesolowski, D. J. Charging Properties of Cassiterite (α -SnO₂) Surfaces in NaCl and RbCl Ionic Media. *Langmuir* **2009**, *25*, 10852–10862.
- (9) Katz, L. E.; Criscenti, L. J.; Chen, C.-c.; Larentzos, J. P.; Liljestrand, H. M. Temperature Effects on Alkaline Earth Metal Ions Adsorption on Gibbsite: Approaches from Macroscopic Sorption Experiments and Molecular Dynamics Simulations. *J. Colloid Interface Sci.* **2013**, *399*, 68–76.
- (10) Předota, M.; Bandura, A. V.; Cummings, P. T.; Kubicki, J. D.; Wesolowski, D. J.; Chialvo, A. A.; Machesky, M. L. Electric Double Layer at the Rutile (110) Surface. 1. Structure of Surfaces and Interfacial Water from Molecular Dynamics by Use of ab Initio Potentials. *J. Phys. Chem. B* **2004**, *108*, 12049–12060.
- (11) Předota, M.; Zhang, Z.; Fenter, P.; Wesolowski, D. J.; Cummings, P. T. Electric Double Layer at the Rutile (110) Surface. 2. Adsorption of Ions from Molecular Dynamics and X-ray Experiments. *J. Phys. Chem. B* **2004**, *108*, 12061–12072.
- (12) Předota, M.; Vlcek, L. Comment on Parts 1 and 2 of the Series “Electric Double Layer at the Rutile (110) Surface. *J. Phys. Chem. B* **2007**, *111*, 1245–1247.
- (13) Zhang, Z.; Fenter, P.; Cheng, L.; Sturchio, N. C.; Bedzyk, M. J.; Machesky, M. L.; Wesolowski, D. J. Model-Independent X-ray Imaging of Adsorbed Cations at the Crystal-Water Interface. *Surf. Sci.* **2004**, *554*, L95–L100.
- (14) Zhang, Z.; Fenter, P.; Cheng, L.; Sturchio, N. C.; Bedzyk, M. J.; Předota, M.; Bandura, A.; Kubicki, J.; Lvov, S. N.; Cummings, P. T.; et al. Ion Adsorption at the Rutile-Water Interface: Linking Molecular and Macroscopic Properties. *Langmuir* **2004**, *20*, 4954–4969.
- (15) Předota, M.; Cummings, P. T.; Wesolowski, D. J. Electric Double Layer at the Rutile (110) Surface. 3. Inhomogeneous Viscosity and Diffusivity Measurement by Computer Simulations. *J. Phys. Chem. C* **2007**, *111*, 3071–3079.
- (16) Parez, S.; Předota, M. Determination of Distance-dependent Viscosity of Mixtures in Parallel Slabs using Non-equilibrium Molecular Dynamics. *Phys. Chem. Chem. Phys.* **2012**, *14*, 3640–3650.
- (17) Machesky, M. L.; Předota, M.; Wesolowski, D. J.; Vlcek, L.; Cummings, P. T.; Rosenqvist, J.; Ridley, M. K.; Kubicki, J. D.; Bandura, A. V.; Kumar, N.; et al. Surface Protonation at the Rutile (110) Interface: Explicit Incorporation of Solvation Structure within the Refined MUSIC Model Framework. *Langmuir* **2008**, *24*, 12331–12339.
- (18) Bonhuis, D. J.; Gekle, S.; Netz, R. R. Profile of the Static Permittivity Tensor of Water at Interfaces: Consequences for Capacitance, Hydration Interaction and Ion Adsorption. *Langmuir* **2012**, *28*, 7679–7694.
- (19) McCafferty, E.; Zettlemoyer, A. C. Adsorption of Water Vapour on α -Fe₂O₃. *Discuss. Faraday Soc.* **1971**, *52*, 239–254.
- (20) Wachter, W.; Buchner, R.; Hefter, G. Hydration of Tetraphenylphosphonium and Tetraphenylborate Ions by Dielectric Relaxation Spectroscopy. *J. Phys. Chem. B* **2006**, *110*, 5147–5154.
- (21) Heugen, U.; Schwaab, G.; Brundermann, E.; Heyden, M.; Yu, X.; Leitner, D. M.; Havenith, M. Solute-induced Retardation of Water Dynamics Probed Directly by Terahertz Spectroscopy. *Proc. Natl. Acad. Sci. U.S.A.* **2006**, *103*, 12301–12306.
- (22) Tielrooij, K. J.; Paparo, D.; Piatkowski, L.; Bakker, H. J.; Bonn, M. Dielectric relaxation Dynamics of Water in Model Membranes Probed by Terahertz Spectroscopy. *Biophys. J.* **2009**, *97*, 2484–2492.
- (23) Teschke, O.; Ceotto, G.; de Souza, E. F. Dielectric Exchange Force: A Convenient Technique for Measuring the Interfacial Water Relative Permittivity. *Phys. Chem. Chem. Phys.* **2001**, *3*, 3761–3768.
- (24) Bernik, D. L.; Negri, R. M. Local Polarity at the Polar Head Level of Lipid Vesicles Using Dansyl Fluorescent Probes. *J. Colloid Interface Sci.* **1998**, *203*, 97–105.
- (25) Bernik, D. L.; Negri, R. M. Critical Revision of Apparent Dielectric Constants Calculations in Lipid–Water Interfaces. *J. Colloid Interface Sci.* **2000**, *226*, 364–366.
- (26) Hiemstra, T.; van Riemsdijk, W. H. *Encyclopedia of Colloid and Interface Science*; Marcel Dekker: New York, 2002.
- (27) Hiemstra, T. Surface Complexation at Mineral Interfaces: Multisite and Charge Distribution approach. Ph.D. Thesis, Wageningen University, 2010.
- (28) Brown, G. E., Jr.; Henrich, V. E.; Casey, W. H.; Clark, D. L.; Eggleston, C.; Felmy, A.; Goodman, D. W.; Grätzel, M.; Maciel, G.; McCarthy, M. L.; et al. Metal Oxide Surfaces and Their Interactions with Aqueous Solutions and Microbial Organisms. *Chem. Rev.* **1999**, *99*, 77–174.
- (29) Hiemstra, T.; Van Riemsdijk, W. H. On the Relationship Between Charge Distribution, Surface Hydration, and the Structure of the Interface of Metal Hydroxides. *J. Colloid Interface Sci.* **2006**, *301*, 1–18.
- (30) Stern, O. The Theory of the Electrolytic Double-Layer. *Z. Elektrochem. Angew. Phys. Chem.* **1924**, *30*, 508–516.
- (31) Wang, H.; Pilon, L. Accurate Simulations of Electric Double Layer Capacitance of Ultramicroelectrodes. *J. Phys. Chem. C* **2011**, *115*, 16711–16719.
- (32) Masliyah, J. H.; Bhattacharjee, S. *Electrokinetic and Colloid Transport Phenomena*; John Wiley and Sons: Hoboken, NJ, 2006.
- (33) Lyklema, J. *Fundamentals of Interface and Colloid Science, Vol. II Solid-Liquid Interfaces*; Academic Press: New York, 1995.
- (34) Rahnemaie, R.; Hiemstra, T.; Van Riemsdijk, W. H. A New Surface Structural Approach to Ion Adsorption: Tracing the Location of Electrolyte Ions. *J. Colloid Interface Sci.* **2006**, *293*, 312–321.
- (35) Sverjensky, D. A. Interpretation and Prediction of Triple-Layer Model Capacitances and the Structure of the Oxide-Electrolyte-Water Interface. *Geochim. Cosmochim. Acta* **2001**, *65*, 3643–3655.
- (36) Sverjensky, D. A. Prediction of Surface Charge on Oxides in Salt Solutions: Revisions for 1:1 (M+L-) Electrolytes. *Geochim. Cosmochim. Acta* **2005**, *69*, 225–257.
- (37) Frydel, D.; Oettel, M. Charged Particles at Fluid Interfaces as a Probe into Structural Details of a Double Layer. *Phys. Chem. Chem. Phys.* **2011**, *13*, 4109–4118.

- (38) Wang, H.; Varghese, J.; Pilon, L. Simulation of Electric Double Layer Capacitors with Mesoporous Electrodes: Effects of Morphology and Electrolyte Permittivity. *Electrochim. Acta* **2011**, *56*, 6189–6197.
- (39) Vorotyntsev, M. A.; Mityushev, P. V. Electric Double Layer Structure in a Surface-Inactive Electrolyte Solution: Effect of the Stern Layer and Spatial Correlations of Solvent Polarization. *Electrochim. Acta* **1991**, *36*, 401–409.
- (40) Finken, R.; Ballenegger, V.; Hansen, J.-P. Onsager Model for a Variable Dielectric Permittivity near an Interface. *Mol. Phys.* **2003**, *101*, 2559–2568.
- (41) Ghoufi, A.; Szymczyk, A.; Renou, R.; Ding, M. Calculation of Local Dielectric Permittivity of Confined Liquids from Spatial Dipolar Correlations. *Europhys. Lett.* **2012**, *99*, 37008.
- (42) Lorenz, C. D.; Crozier, P. S.; Anderson, J. A.; Traveset, A. Molecular Dynamics of Ionic Transport and Electrokinetic Effects in Realistic Silica Channels. *J. Phys. Chem. C* **2008**, *112*, 10222–10232.
- (43) Pandit, S. A.; Bostick, D.; Berkowitz, M. L. An Algorithm to Describe Molecular Scale Rugged Surfaces and Its Application to the Study of a Water/Lipid Bilayer Interface. *J. Chem. Phys.* **2003**, *119*, 2199–2205.
- (44) Lin, J.-H.; Baker, N. A.; McCammon, J. A. Bridging Implicit and Explicit Solvent Approaches for Membrane Electrostatics. *Biophys. J.* **2002**, *83*, 1374–1379.
- (45) Stern, H. A.; Feller, S. E. Calculation of the Dielectric Permittivity Profile for a Nonuniform System: Application to a Lipid Bilayer Simulation. *J. Chem. Phys.* **2003**, *118*, 3401–3412.
- (46) Wander, M. C. F.; Clark, A. E. Structural and Dielectric Properties of Quartz-Water Interfaces. *J. Phys. Chem. C* **2008**, *112*, 19986–19994.
- (47) Frenkel, D.; Smit, B. *Understanding Molecular Simulation: From Algorithms to Applications*; Academic Press: London, 2002.
- (48) Kirkwood, J. G. The Dielectric Polarization of Polar Liquids. *J. Chem. Phys.* **1939**, *7*, 911–919.
- (49) Ballenegger, V.; Hansen, J.-P. Dielectric Permittivity Profiles of Confined Polar Fluids. *J. Chem. Phys.* **2005**, *122*, 114711 1–10.
- (50) Bonhuis, D. J.; Gekle, S.; Netz, R. R. Dielectric Profile of Interfacial Water and its Effect on Double-Layer Capacitance. *Phys. Rev. Lett.* **2011**, *107*, 166102 1–5.
- (51) Jackson, J. D. *Classical Electrodynamics*; John Wiley and Sons: New York, 1998.
- (52) Faraudo, J. The Missing Link Between the Hydration Force and Interfacial Water: Evidence from Computer Simulations. *Curr. Opin. Colloid Interface Sci.* **2011**, *16*, 557–560.
- (53) Yeh, I.; Berkowitz, M. L. Dielectric Constant of Water at High Electric Fields: Molecular Dynamics Study. *J. Chem. Phys.* **1999**, *110*, 7935–7942.
- (54) Abascal, J. L. F.; Vega, C. A General Purpose Model for the Condensed Phases of Water: TIP4P/2005. *J. Chem. Phys.* **2005**, *123*, 234505 1–12.
- (55) Vega, C.; Abascal, J. L. F. Simulating Water with Rigid Non-Polarizable Models: A General Perspective. *Phys. Chem. Chem. Phys.* **2011**, *13*, 19663–19688.
- (56) Steele, W. A. *The Interaction of Gases with Solid Surfaces*; Pergamon Press: Oxford, 1974.
- (57) Bandura, A. V.; Kubicki, J. D. Derivation of Force Field Parameters for TiO₂-H₂O Systems from ab Initio Calculations. *J. Phys. Chem. B* **2003**, *107*, 11072–11081.
- (58) Yeh, I.; Berkowitz, M. L. Ewald Summation for Systems with Slab Geometry. *J. Chem. Phys.* **1999**, *111*, 3155–3162.
- (59) Nosé, S. A Unified Formulation of the Constant Temperature Molecular Dynamics Methods. *J. Chem. Phys.* **1984**, *81*, 511–519.
- (60) Hoover, W. G. Canonical Dynamics: Equilibrium Phase-Space Distributions. *Phys. Rev. A* **1985**, *31*, 1695–1697.
- (61) Flyvbjerg, H.; Petersen, H. G. Error Estimates on Averages of Correlated Data. *J. Chem. Phys.* **1989**, *91*, 461–466.
- (62) Fröhlich, H. *Theory of Dielectrics*; Clarendon Press: Oxford, 1949.
- (63) Předota, M.; Nezbeda, I.; Parez, S. Coarse-Grained Potential for Interaction with a Spherical Colloidal Particle and Planar Wall. *Collect. Czech. Chem. Commun.* **2010**, *75*, 527–545.
- (64) Předota, M.; Machesky, M. L.; Wesolowski, D. J.; Cummings, P. T. Electric Double Layer at the Rutile (110) Surface. 4. Effect of Temperature and pH on the Adsorption and Dynamics of Ions. *J. Phys. Chem. C* **2013**, *117*, 22852–22866.
- (65) Ridley, M. K.; Hiemstra, T.; van Riemsdijk, W. H.; Machesky, M. L. Inner-Sphere Complexation of Cations at the Rutile–Water Interface: A Concise Surface Structural Interpretation with the CD and MUSIC Model. *Geochim. Cosmochim. Acta* **2009**, *73*, 1841–1856.
- (66) Booth, F. The Dielectric Constant of Water and the Saturation Effect. *J. Chem. Phys.* **1951**, *19*, 391–394.
- (67) Aguilera-Arzo, M.; Andrio, A.; Aguilera, V. M.; Alcaraz, A. Dielectric Saturation of Water in a Membrane Protein Channel. *Phys. Chem. Chem. Phys.* **2009**, *11*, 358–365.